machines

MDPI

Article

Development of a Hydraulic Conical Valve for the Linearization of Flow

Suyambu Pandian Asok [1,*], Balasubramanian Vijayaragavan [1], Thirumalachari Sundararajan [2] and Gurunathan Rajaguru Manikandan [3]

[1] Department of Mechanical Engineering, Mepco Schlenk Engineering College, Sivakasi 626005, India
[2] Department of Mechanical Engineering, Indian Institute of Technology, Palakkad 678623, India
[3] Tata Consultancy Services, 40472 Düsseldorf, Germany
* Correspondence: spasok@mepcoeng.ac.in

Abstract

Conventional throttling valves have non-linear flow characteristics. However, in precise processes of flow control requiring them, appropriate flow modulations are necessary to enable a linear flow response even under partial valve actuations. This paper formulates a hydraulic conical valve configuration that exhibits linear flow. Flow studies were conducted on a 24 mm orifice-sized Conventional Conical Valve (CCV) using Computational Fluid Dynamics (CFD) analysis with commercial code ANSYS Fluent 2022 R1 and through experiments. The mass flow curve for the CCV had a convex upward shape, implying that at all valve openings, its discharges lay above the linear discharge line. To create greater resistance to flow, a venturi was incorporated into the valve casing close to the downstream side of the valve seat, leading to a Venturi Conical Valve (VCV). CFD analysis revealed that the addition of the venturi added more flow resistance, while the identified optimal VCV was still unable to make the flow linear. Subsequently, labyrinth cavities were machined on the conical valve body of the VCV, changing it into a Labyrinth Venturi Conical Valve (LVCV). Experiments revealed that the discharge curve for the identified LVCV was nearly linear. The maximum linearity deviation of 45.76% found in the CCV decreased to 9.95% in the LVCV. The reduction in linearity deviation indicates an improved closeness of the valve discharge to the linear conditions.

Keywords: flow linearization; control valve; labyrinth; venturi; CFD

check for updates

Academic Editor: Zheng Chen

Received: 24 July 2025
Revised: 29 August 2025
Accepted: 1 September 2025
Published: 18 September 2025

Citation: Asok, S.P.; Vijayaragavan, B.; Sundararajan, T.; Manikandan, G.R. Development of a Hydraulic Conical Valve for the Linearization of Flow. *Machines* **2025**, *13*, 866. https://doi.org/10.3390/machines13090866

Copyright: © 2025 by the authors. Licensee MDPI, Basel, Switzerland. This article is an open access article distributed under the terms and conditions of the Creative Commons Attribution (CC BY) license (https://creativecommons.org/licenses/by/4.0/).

1. Introduction

Control valves are widely used in pipe systems to vary flow rate as well as pressure. They have predominantly non-linear flow or quick-opening characteristics and are mainly used for controlling pressure. Valves having linear characteristics are applicable where most of the system pressure drop occurs at the valve. Such valves are imperative in close flow and control process industries [1]. In applications like liquid flow through the bypass valve of a nuclear reactor and cryogenic rocket engine components, linear control of flow is an important design issue, which is investigated in this paper for a conical valve. Conventional hydraulic control valves have quick-opening-type characteristics [2] and suffer from poor controllability in that flow rises very steeply with early opening values. Through most of the latter part of the opening range, they have very little effect on the flow rate passing through them. Our quest herein is for a valve wherein the mass flow rate changes linearly with the position of the valve plug throughout the entire operating range. Such a valve

necessitates that the valve plug be rapidly tapered for the promotion of linear discharge [3]. Linearization studies were conducted on ball valves by applying V-ports, which, however, increased the tendency for cavitation [4]. For better flow control, the design of the valve requires it to be a significant restrictor in the flow stream even when in the fully open condition [5], which demands further technical developments.

Control valve characteristics are typically difficult to determine using empirical correlations and dimensional analysis methods. Analytical expressions are applicable only to the fully opened condition of the valves and are not commonly used for flow control. Flow through valves is complex, and better understanding of valve characteristics demands applied technologies such as particle image velocimetry and CFD flow simulations [6]. The former technique requires numerous time-consuming test runs and is expensive. Dependable computational modeling of valves, in addition to saving cost and time, also provides safer valve designs. Commercial CFD code ANSYS Fluent [7] and experiments were employed to analyze flow through control valves. The axisymmetric k-ε CFD turbulence model was able to make predictions across a large range of valve openings [8,9].

The following are the prominent research gaps in the context of water flow through Conventional Conical Valves in the open literature, arising out of the unavailability of the following: flow restrictors, flow linearization attempts, and the role of vortices downstream of the valve. At the backdrop of these, the present paper addresses the same alongside novel design modifications like bringing in a new flow-impediment component into the assembly viz. a venturi, sizing and appropriately positioning it with reference to the conical valve plug, which in turn is implemented with labyrinth grooves on its body. All these efforts were focused on enabling the flow appreciably close to being linear.

2. CFD Analysis for Flow Linearization

2.1. Conventional Conical Valve (CCV)

Figure 1 shows the Conventional Conical Valve (CCV) considered in the current work. These valves have a maximum stroke of 16 mm, beyond which there has been no noticeable change in discharge. The valve position is expressed as a percentage, representing the ratio between the actual and maximum strokes. Examination of the liquid flow passage through the valve seat and body of the CCV indicates axisymmetric regions. The commercial finite volume CFD code ANSYS Fluent 2022 R1 was used to perform CFD analysis. Considering simplicity, axisymmetric CFD analysis was predominantly carried out [6,10] at various valve openings, primarily in steps of 10%.

For axisymmetric analysis, the symmetrical condition was imposed at the valve centerline passing through the cone's apex, and the flow domain was discretized using triangular elements with a refinement option, which created meshes consisting of irregular triangular elements. Neither energy transfer nor change in fluid temperature was involved. Additionally, the parameters for all simulation models corresponding to each valve opening were kept constant. It is common to notice that flow boundary conditions are employed to have uniform velocity and pressure at the inlet and exit, respectively [11]. Yet, the current study is concerned with situations where the constant inlet pressure upstream of the valve and the exit pressure downstream of the valve, which is atmospheric, are the known parameters at any value of valve opening. Hence, it was more prudent to impose pressures at the extremities [12] of the valve.

Accordingly, a uniform gauge pressure of 5 bar at the inlet and 0 bar at the exit were taken as the boundary conditions for the CFD analysis in this work, and the same were maintained during the experiments as well. No pressure profile was defined at the inlet, and the values were kept constant for all cases. To overcome flow disturbances caused by the entry section, a pressure gauge was installed in a straight run of the inlet pipe at a

distance of four times the pipe inner diameter ahead of the valve apex. All solid surfaces of the flow passage were imposed with no slip velocity. Since the experimental Reynolds numbers for the CCV conveyed turbulent flow conditions, the Reynolds-averaged Navier–Stokes (RANS) model was chosen in this work for the numerical analysis [13], using the standard k-ε model to simulate the turbulence characteristics of the flow [14].

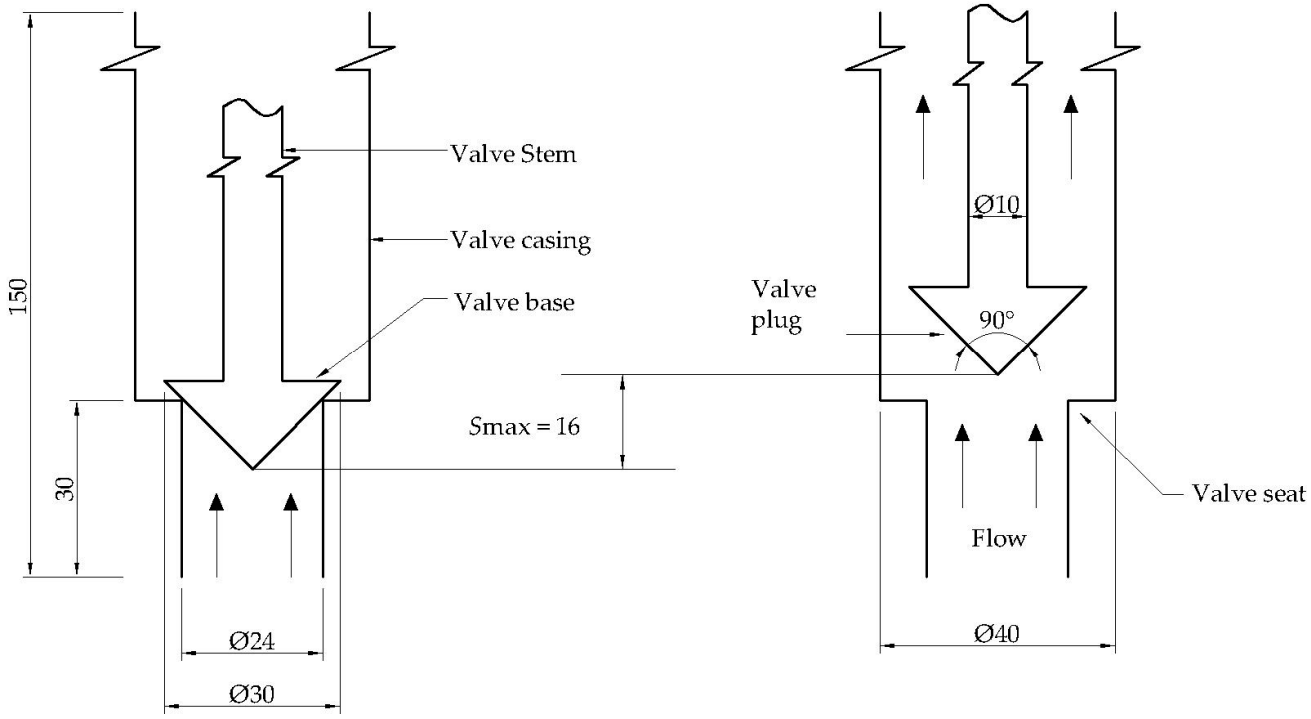

Figure 1. Diagrams showing CCV in fully closed and fully open conditions (units in mm).

Considering the computational domain being relatively small, the values of k and ε at the inlet were not estimated using formulae. The default k and ε parameters of the ANSYS Fluent program were used in the model. A turbulent intensity of 10% was set at the inlet. The near-wall features were defined using logarithmic wall functions. The second-order upwind SIMPLEC algorithm was used to obtain the numerical solutions. The axisymmetric mesh employed for the current analysis is shown in Figure 2 for a 10% valve opening condition. Since higher grid concentrations around the valve seat region would lead to improved resolution of vortices and a separated boundary layer, these meshes were successively refined closer to the walls [15]. The residuals were fixed at four orders of magnitude for the convergence criteria.

Improved results were realized when wall y plus values for grid points near the wall varied from 1.5 to 25 [16]; see Figure 3. This refinement process simultaneously accounted for conducting a grid independence test and was stopped when successive grids were almost yielding the same value of mass flow rate. The dimensionless mass flow ratio (m) is obtained by dividing the mass flow rate by a reference value. As seen in Table 1, there was a very minimal change in the value of maximum velocity (Vmax) across the range of cells, starting from 49,404 and ending at 117,438, for the 100% valve opening condition. The CPU solution times had risen during mesh refinement. The convergence of the solution required approximately 2500 s of CPU time on an Intel Core i5, 8 GB RAM computer.

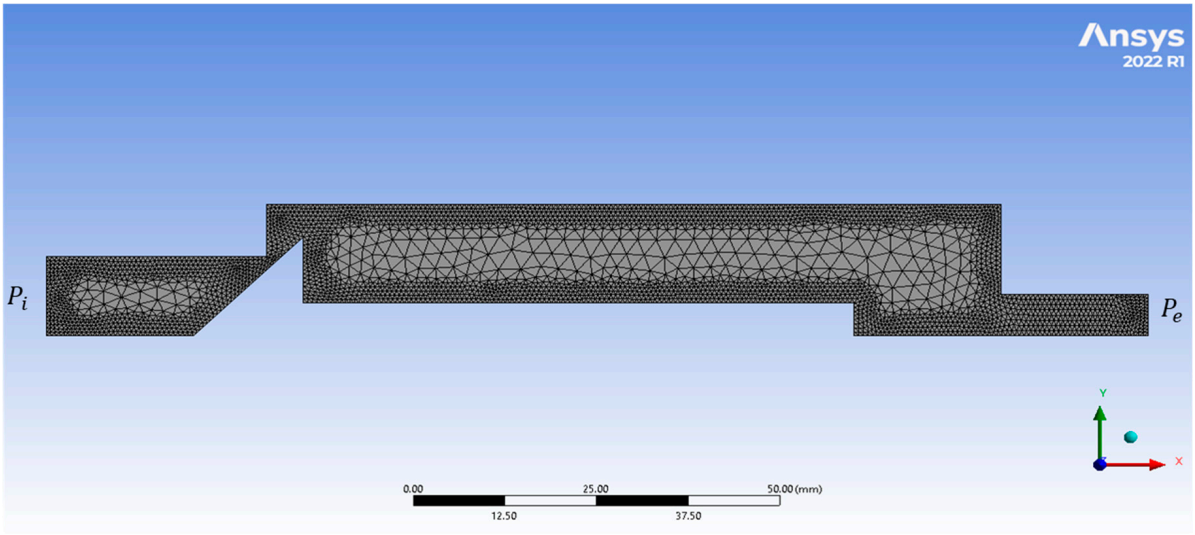

Figure 2. The computational mesh for the 10% valve opening of the CCV (Pi—inlet gauge pressure; Pe—exit atmospheric pressure).

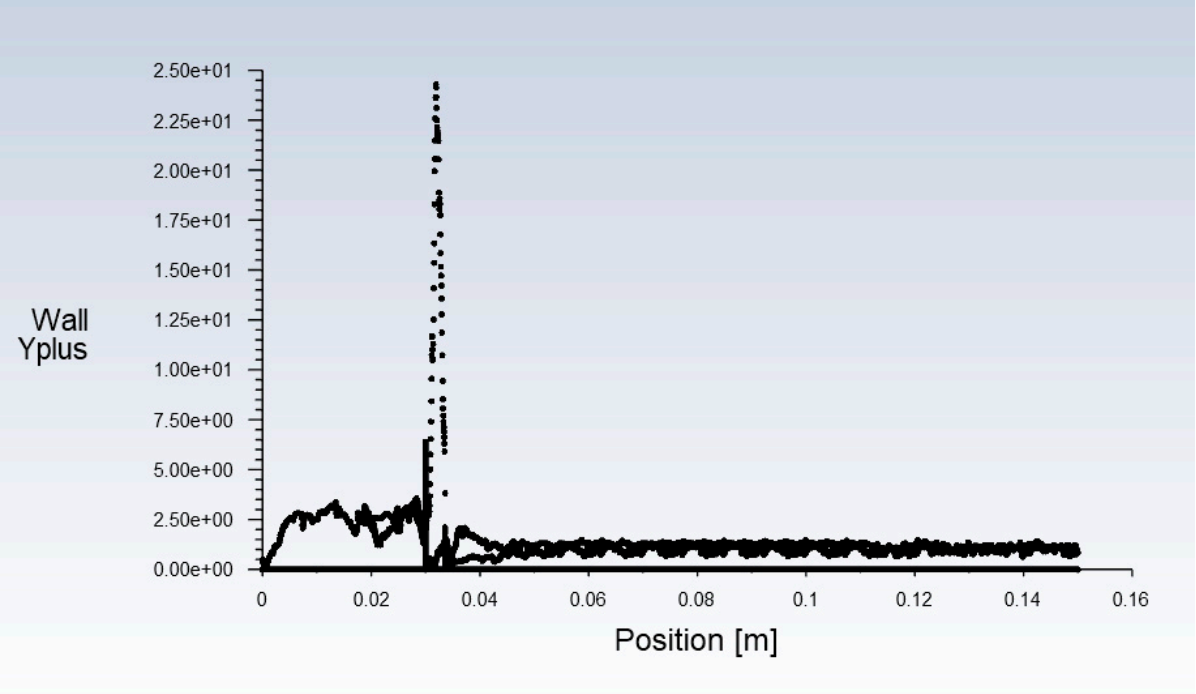

Figure 3. Wall y plus values at 10% valve opening of CCV.

Table 1. Axisymmetric CFD prediction of CCV's maximum velocity at 100% valve opening.

Cells	49,404	67,696	103,392	117,438
V_{max} in m/s	31.6	31.5	32.2	32.3

Figure 4 provides the mass flow ratios predicted by CFD at various valve openings of the CCV, along with the corresponding values at linear opening conditions. It confirms that the CCV has a non-linear, quick opening, and convex upwards variation in mass flow against different valve openings of the CCV in increments of 10%.

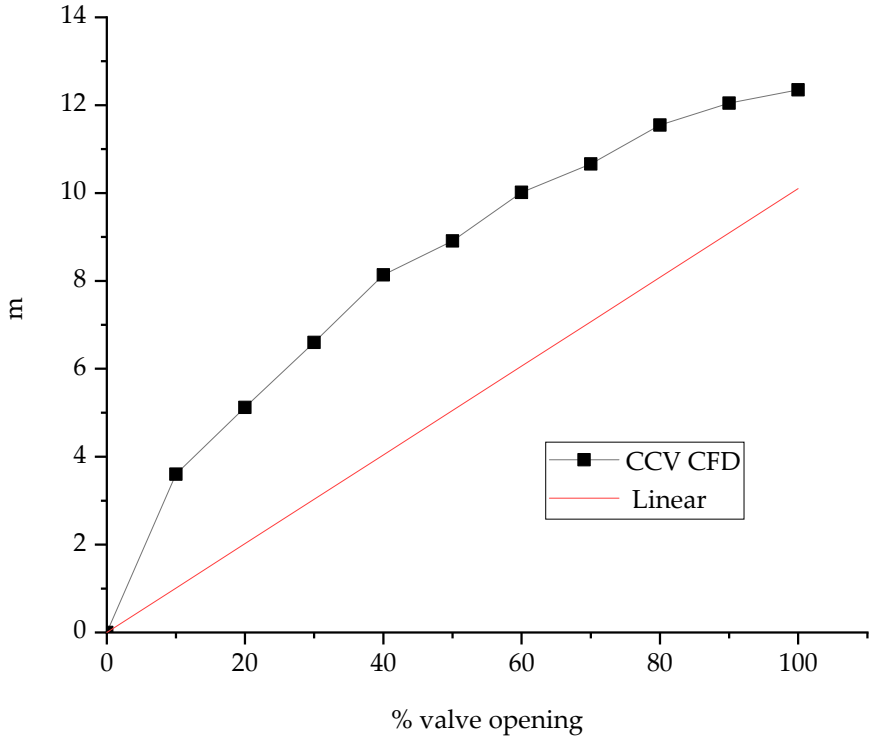

Figure 4. Axisymmetric CFD-predicted mass flow ratios of CCV.

Figure 5a shows the velocity vectors in the valve region of the CCV. It can be noticed that the flow accelerates through the entrance of the valve opening, the slant valve body, and up to the valve base area where the vena contracta exists. Since the section is relatively short, the discussed flow field in the vena contracta area can be speculated to be very strong. The predominant maximum flow velocity exists at the vena contracta, which is plotted against different valve openings in Figure 5b. Just after passing the valve gap at the valve seat, the flow partially becomes free of the wall effects, and the flow jet splits into two portions. One is the main jet flowing out in the downstream direction, while the other is the separated shear layer. The latter forms a recirculation zone just adjacent to the valve seat in the corner region and in the vicinity of the vena contracta, which is named the primary vortex.

After passing the valve base, the main jet fluid is seen attached to the valve casing's inner wall, traveling axially. In the downstream direction, a portion of it moves towards the valve stem, forming a single large recirculation region, which is termed the secondary vortex. Figure 5a also shows four location points, L1, L2, L3, and L4. The first location point L1 was chosen to be at the epicenter of the primary vortex, and the remaining location points lie on a vertical straight line passing through the axis of rotation of the bigger secondary vortex. Figure 5c shows the velocity values at these four location points for the CCV at different valve openings. The velocity values at L1 and L3 are very low due to near stagnation in the center of the primary and secondary vortices. The highest velocity value at L2 indicates the flow of the main jet along with the recirculating jet in the vortex, which is non-monotonous in the higher valve opening range due to the influence of the main jet. The lower value of velocity at L4 compared to L2 is due to the presence of the recirculating jet alone. In Figure 5d, the velocity profiles on two vertical planes passing through L1 and the remaining location points, L2, L3, and L4, are shown at the 100% CCV valve opening, obtained using axisymmetric analysis. The negative components show the flow reversal corresponding to the vortex flows in the valve.

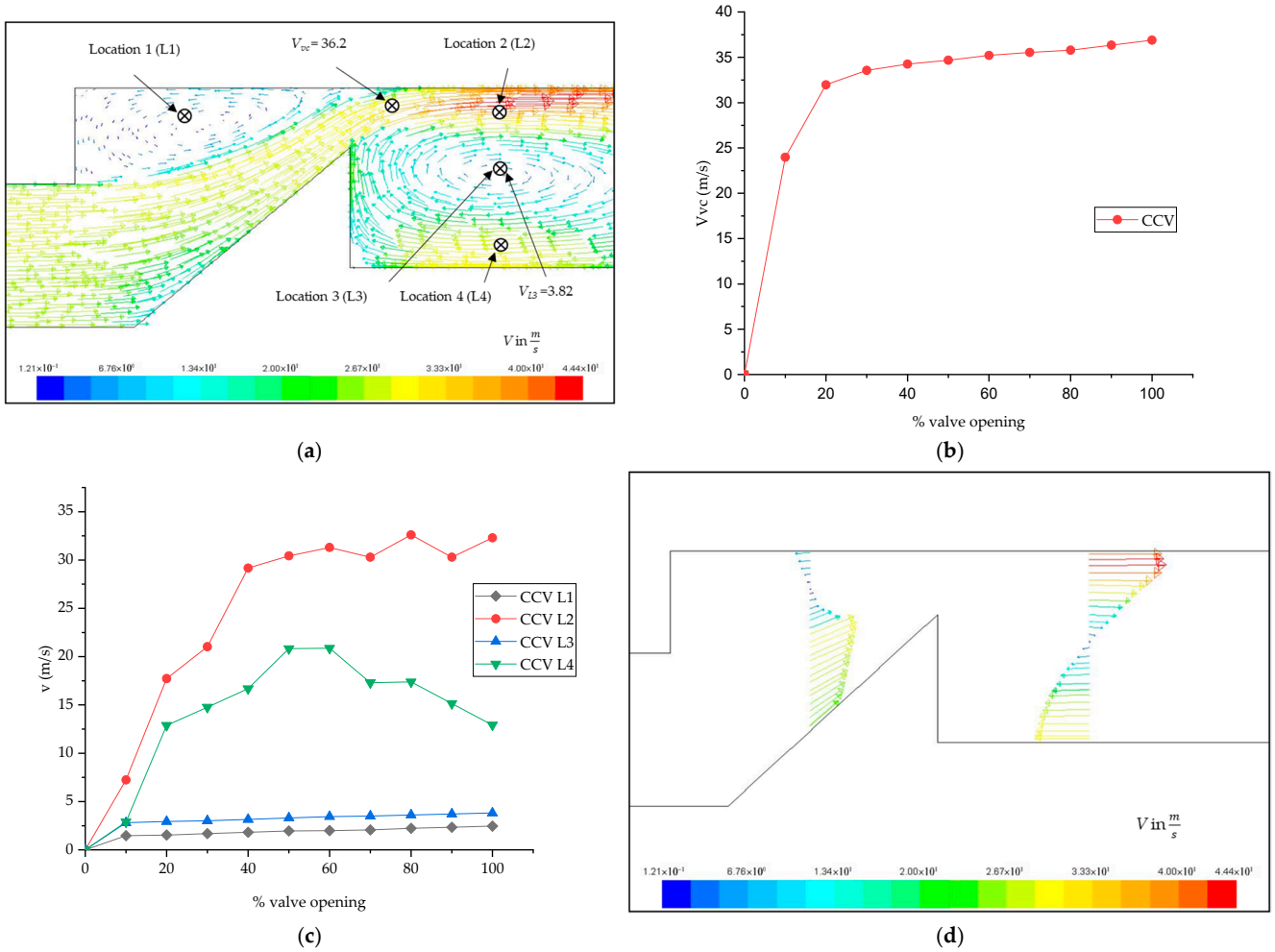

Figure 5. (**a**) Axisymmetric CFD analysis: velocity vectors, V_{vc}, and V_{L3} and indication of four location points for CCV at 100% opening. (**b**) Axisymmetric CFD analysis: V_{vc} vs. % valve opening for CCV. (**c**) Axisymmetric CFD analysis: velocities at the four locations shown in (**a**) for CCV vs. % valve opening. (**d**) Axisymmetric CFD analysis: velocity vector for CCV at 100% opening on the vertical plane along the four locations.

At the vena contracta zone immediately following the valve seat area, local energy losses occur due to the presence of swirls. The values of turbulent kinetic energy (k) in both the primary and secondary recirculation regions are seen in Figure 6a for a valve opening of 75%. Figure 6b shows the k values at the four location points for the CCV at different valve openings. Among these values, the values associated with the first location point lying in the primary vortex zone are the lowest. The values at locations two and four are comparable and occur in proximity to the walls. The value at location three is the maximum since high eddy dissipation losses occur in that large recirculation zone. Additionally, it is worth noting that these losses are rising steeply up to around a valve opening of 40%, beyond which the increase is minimal. This indicates that these losses become nearly independent of the Reynold's number beyond the latter's value of 4×10^5. Figure 7 indicates the stream function (Ψ) values in both the recirculation regions for a valve opening of 50%. The static pressure contours at a valve opening of 25% are shown in Figure 8a, and static pressure values at the vena contracta of the CCV at different valve openings are given in Figure 8b.

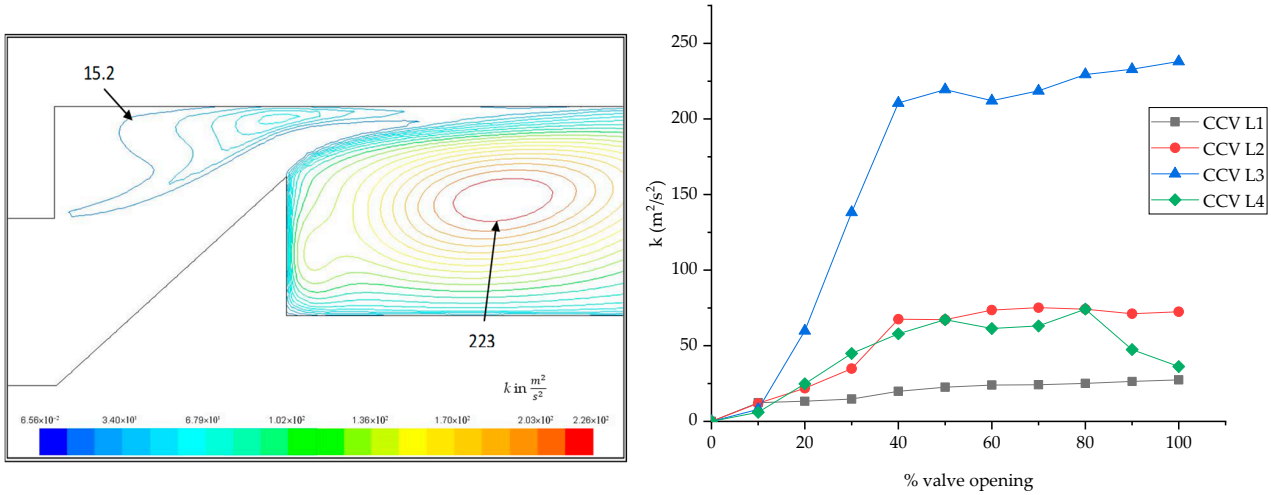

(**a**) (**b**)

Figure 6. (**a**) Axisymmetric CFD analysis: contours of k for CCV at 75% opening. (**b**) Axisymmetric CFD analysis: k values at the four locations shown in Figure 5a for CCV vs. % valve opening.

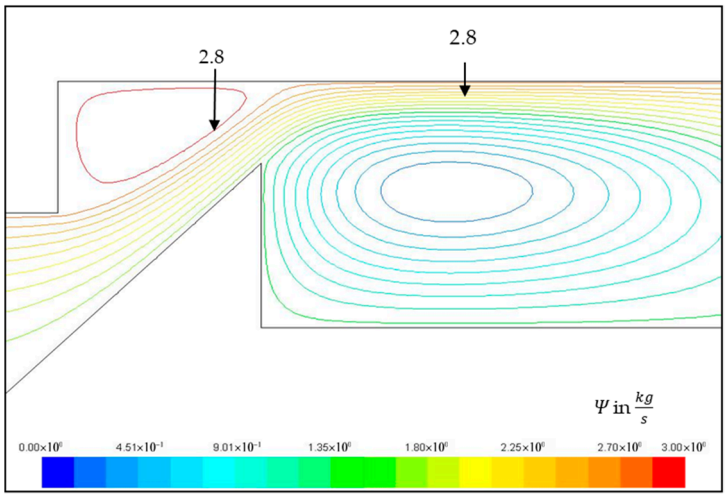

Figure 7. Axisymmetric CFD analysis: contours of stream function for CCV at 50% opening.

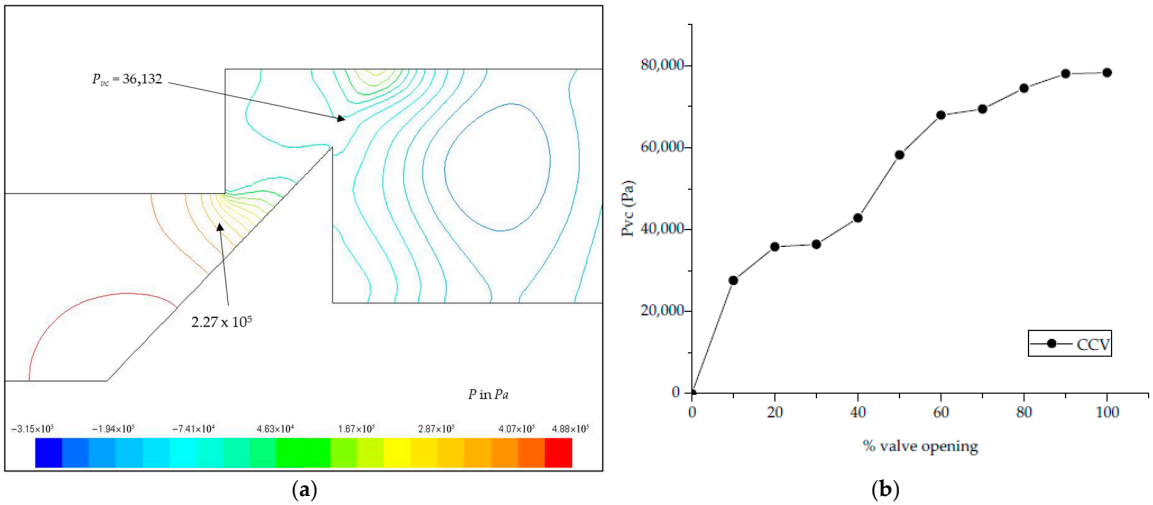

(**a**) (**b**)

Figure 8. (**a**) Axisymmetric CFD analysis: contours of static pressure for CCV at 25% opening. (**b**) Axisymmetric CFD analysis: vena contracta static pressures of CCV vs. % valve opening.

Falling back on Figure 4, the linear mass flow line superimposed clearly indicates that at all valve openings, the flow of the CCV is higher than the linear curve by differing quantities. It is obvious that to linearize the flow, the valve should be equipped with appropriate higher flow resistances at all valve openings. This paper subsequently moves on to focus on the efforts taken towards the same.

2.2. Venturi Conical Valve (VCV)

Following the report that the effect of the valve plug's cone angle was diminished on mass flow for valve openings beyond 70% [17], a design change was contemplated on the casing of the valve. Helical profiles capable of creating a venturi effect were employed in a flow passage, which caused more minor flow losses and further enhanced flow resistance [18]. Accordingly, a venturi profile was incorporated into the CCV setup, resulting in the Venturi Conical Valve (VCV) shown in Figure 9. The venturi's presence was expected to increase the strength of the vortex formed in the vena contracta zone (secondary vortex), thus helping the cause of linearization by flattening the discharge curve seen in Figure 10, i.e., transforming the arc variation into a straight-line pattern. After performing a preliminary parametric CFD analysis, the length of the venturi was fixed at the same value as the maximum stroke of the valve, i.e., 16 mm. Also, the favorable location for the venturi was found to be such that at the fully open condition of the valve, both the downstream base of the venturi and the base of the valve would lie on a single plane perpendicular to the centerline of the valve. Under the above conditions, three different VCVs having throat diameters as specified in Table 2 were analyzed using CFD.

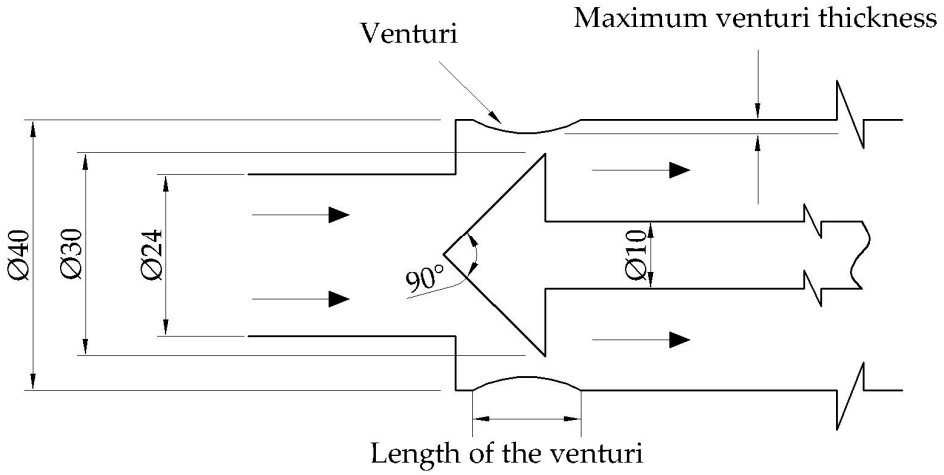

Figure 9. Venturi Conical Valve (VCV) (units in mm).

Table 2. Throat diameters of three VCVs.

Sl. No.	Name of VCV	Throat Diameter in mm
1.	VCV-1	37
2.	VCV-2	35
3.	VCV-3	34

As seen in Figure 10, a significant amount of additional flow resistance is available with the three VCVs in the valve opening range of 50% to 80%. In fact, the mass flow rate of VCV-3 at nearly 70% opening of the valve has just reached the linear CCV mass flow rate line. Hence, any VCV having a minimum throat diameter of below 34 mm was not considered for further analysis. Overall, the VCV-3 is the optimal VCV since it offered the highest additional resistance to the flow and caused the lowest mass flow rates at various

valve openings. While the mass flow rate for VCV-3 between the 70% and 100% valve opening(s) follows a linear path, the same between 0% and 70% still had a convex upwards variation, viz., a quick opening characteristic. Hence, suitable additional resistance had to be provided to the VCV-3 configuration in the non-linear region.

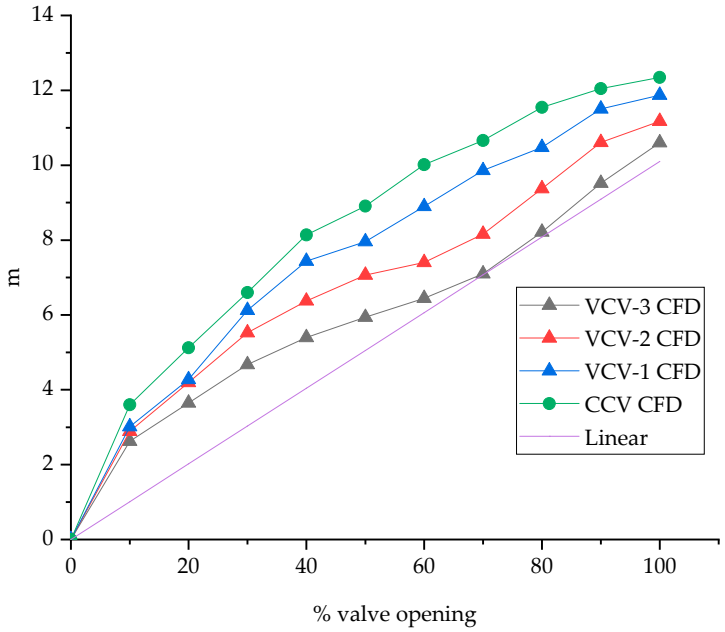

Figure 10. Axisymmetric CFD-predicted mass flow ratios of CCV and VCVs.

At the different valve openings considered, the vena contracta velocity (Vvc) and vena contracta pressure (Pvc) values of the VCV compared to those of the CCV were higher. The representative values at the 100% valve opening are shown in Table 3. The four location points indicated in Table 4 are those lying on VCV-3 at similar positions indicated earlier for the CCV. From Table 4, where the entries correspond to the 100% valve opening, it can be observed that the value of turbulent kinetic energy (k) at L1 for the VCV is less than that for the CCV. At the remaining three location points, the k values are higher for the VCV, which means enhanced flow resistance. Still, the discharge curve for the optimal VCV-3 given in Figure 10 was found to fall short of creating enough flow resistance needed to reach the linear natured curve.

Table 3. Vena contracta velocities (in m/s) and pressures (in Pa) for CCV and VCV at s = 100%.

% Valve Opening	CCV		VCV	
	V_{vc}	P_{vc}	V_{vc}	P_{vc}
100	36.20	78,296	36.70	81,453

Table 4. Local values of k (in m^2/s^2) for CCV and VCV at s = 100%.

Sl. No	Location	CCV	VCV
		k	k
1	L1	27.41	24.63
2	L2	72.51	77.37
3	L3	238.01	244.11
4	L4	36.28	47.66

2.3. Labyrinth Venturi Conical Valve (LVCV)

For the same mass flow rate, a valve passage with labyrinths exhibits enhanced flow resistance, resulting in a higher pressure drop compared to the passage without labyrinths [19]. Conversely, under the same inlet and exit pressure conditions, as is the case with the valves discussed here, a valve passage with labyrinths would permit a lower mass flow rate. The fluid entrapped in the labyrinth chambers on the valve body is forced to undergo vortex motion. The vortices repel the movement of passing fluid. Additionally, the labyrinth section reduces the mass flow by converting the pressure energy to kinetic energy, which is subsequently dissipated into heat at the labyrinth chambers [20]. Further, labyrinth chambers on a valve body enable the flow area even closer to the valve seat region to open up more, which contributes to enhanced flow resistance and higher losses.

The above discourse was applied in the present work since a valve configuration discharging less than the VCV was required. Pressure reduction would take place smoothly in the flow through a conical valve incorporating labyrinth cavities, whereas pressure would sharply drop in the valve base region of a CCV. Hence, square-shaped labyrinth cavities were machined on the tapering conical valve body of VCV-3. The relative geometry of the configuration was kept such that there were as many practically sized labyrinth grooves as possible. Also, to prevent leakage, no labyrinth cavity was created to interfere with the valve seat at the completely closed condition of the valve.

Further, at very low valve openings, say up to 5% in a CCV, having no additional flow resistance at the slant valve body, there would be a dramatic fall in pressure in the vicinity of the vena contracta region immediately downstream to the valve seat. But in an LVCV, the labyrinth cavities on the slant valve body would have already started to diminish some pressure due to vortex losses inside the cavities. This is envisaged to make the pressure drop happen immediately after the valve seat, not to be so sudden as was the case with the CCV. This was how the Labyrinth Venturi Conical Valve (LVCV) configuration, shown in Figure 11, was formulated.

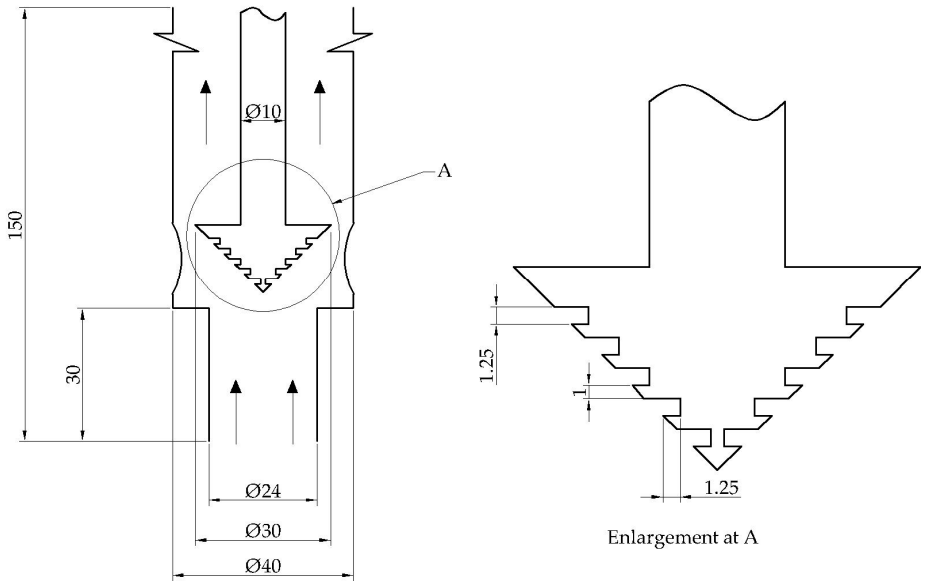

Figure 11. LVCV at fully open condition (units in mm).

Similar to the CCV, a very minimal change in the value of maximum velocity (Vmax) is obtained for the mesh model with 118,808 cells for the 100% valve opening condition. The refined axisymmetric mesh of the LVCV for 10% valve opening is seen in Figure 12. Four location points on the LVCV at similar locations to the CCV are shown in Figure 13a.

Figure 13b showing the relative variations in Vvc of the CCV and LVCV at different valve openings presents a picture of the complex flow dynamics existing in the zone ranging from the valve seat to the base edge of the valve plug, interfered with by the protruding venturi.

The trend of velocity variations at the four location points is drawn in Figure 13c. The values for both the CCV and LVCV are more or less the same at the centers of the primary and secondary vortex regions (L1 and L3). But the combined effect of the labyrinth and venturi is found at locations L2 and L4, whereby the velocities of the LVCV clearly exceed that of the CCV. This implies the existence of a stronger secondary vortex in the LVCV.

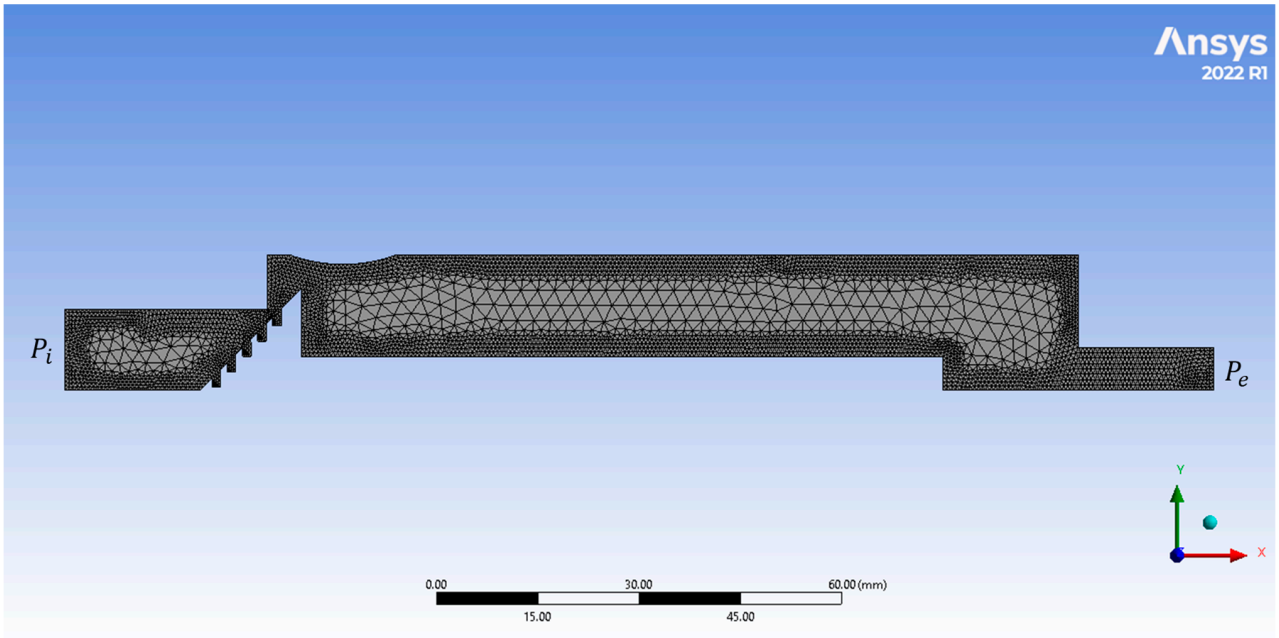

Figure 12. The computational mesh for the 10% valve opening of the LVCV (Pi—inlet gauge pressure; Pe—exit atmospheric pressure).

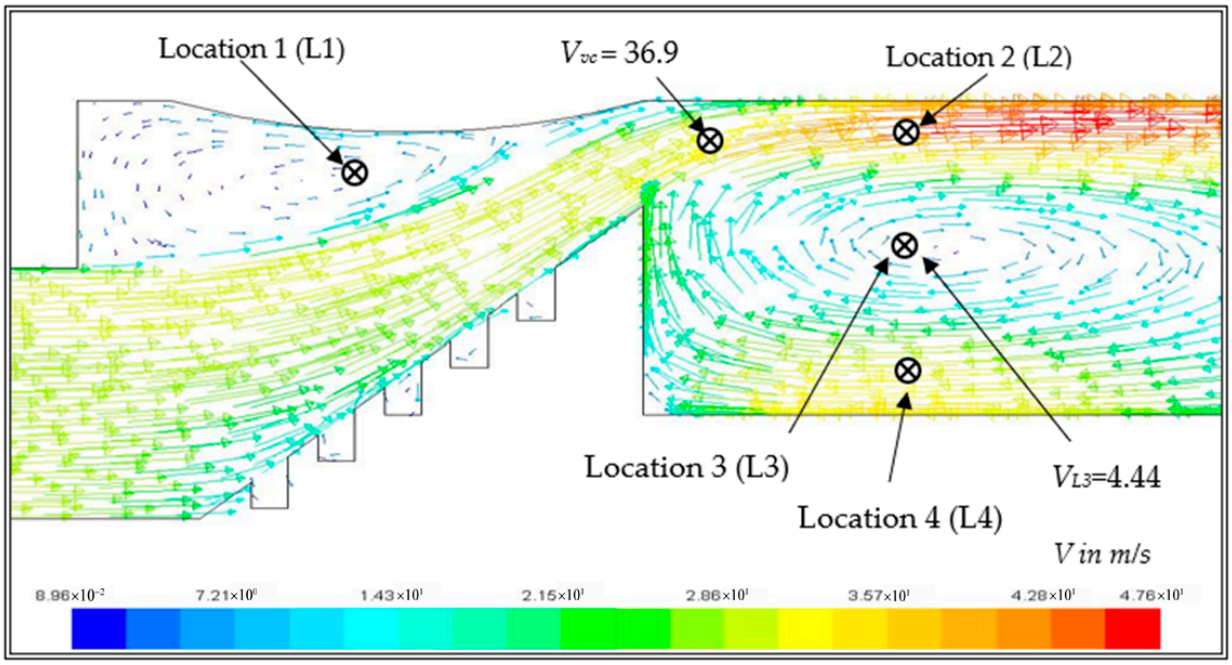

(**a**)

Figure 13. *Cont.*

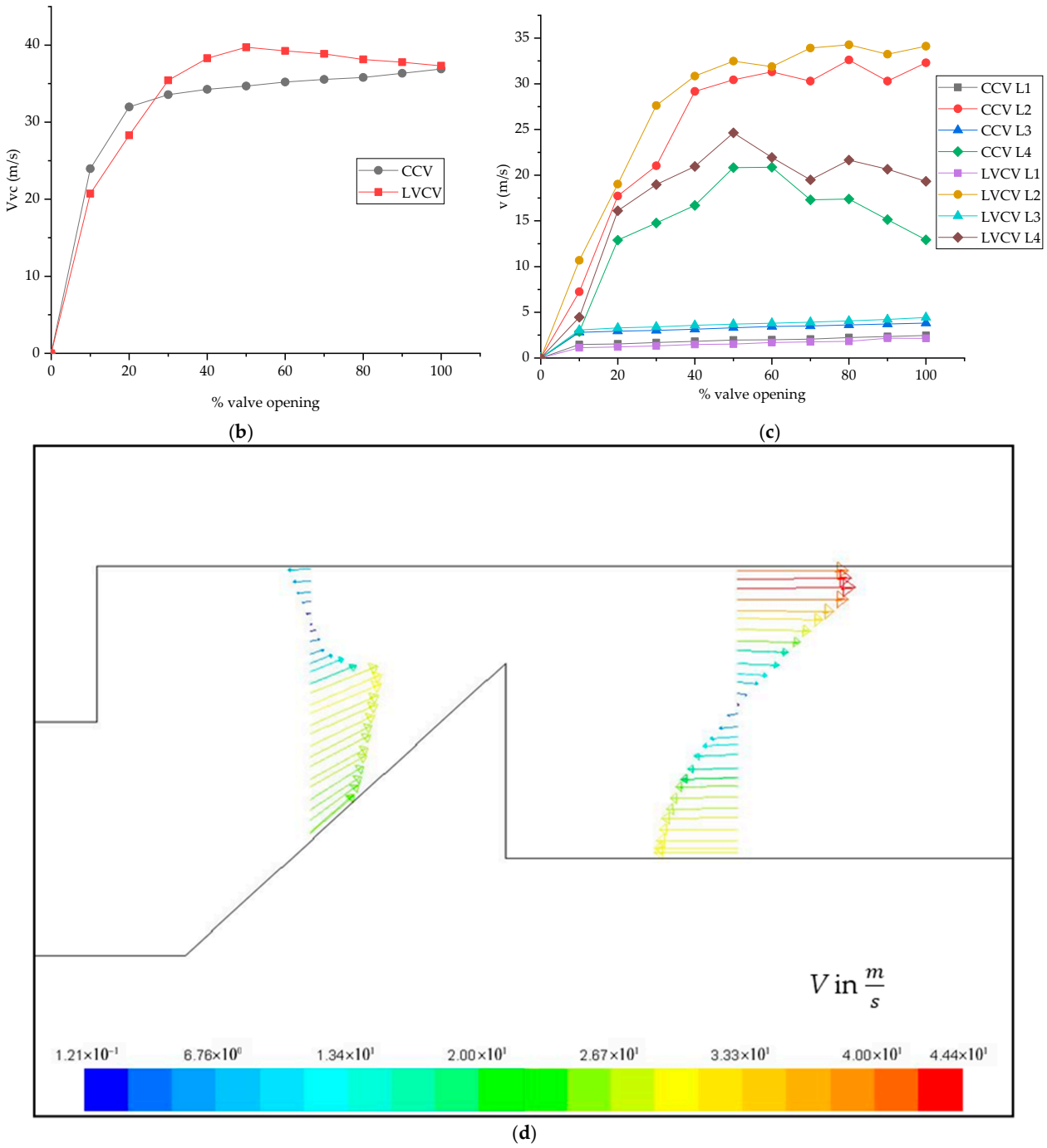

Figure 13. (**a**) Axisymmetric CFD analysis: velocity vectors, V_{vc} and V_{L3} and indication of four location points for the LVCV at the 100% opening. (**b**) Axisymmetric CFD analysis: V_{vc} vs. % valve opening for the LVCV and CCV. (**c**) Axisymmetric CFD analysis: (i) velocities at the four locations shown in (**a**) for the LVCV vs. % valve opening; (ii) velocities at the four locations shown in Figure 5a for the CCV vs. % valve opening. (**d**) Axisymmetric CFD analysis: velocity vector for the LVCV at the 100% opening on the vertical plane along the four locations.

At s values up to about 25%, the CFD values of Vvc for the LVCV are less than those for the CCV. This is because, during this stage, in addition to the flow resistance caused by the labyrinth cavities, further obstruction was created by the back pressure caused by impingement of the flowing fluid on the impending converging part of the venturi.

For s values ranging from around 25% to 50% of the LVCV, the flow is further narrowed down towards the least cross-sectional area as the crest of the venturi comes into play. This

results in overshooting of the Vvc to a maximum, which is well beyond the maximum Vvc of the CCV. During further valve openings, as the flow relatively eases past the diverging part of the venturi, which is now apparent, the Vvc values of the LVCV start declining due to Bernoulli's effect brought about by the increasing flow area.

Figure 13d shows the velocity vectors of the LVCV for the 100% valve opening on the vertical plane along the four location points shown in Figure 13a. A comparison of Figure 13d with Figure 5d indicates that in both the LVCV and CCV, the fluid flow patterns are similar, with the fluid leaving the valve base zones essentially as a wall jet.

The variations in k for the LVCV at the four location points shown in Figure 13a and the k values at each of the centers of the vortices for the LVCV are shown in Figures 14a and 14b, respectively. At location L1 lying in the middle of the primary vortex, the k value for the LVCV is less than that for the CCV due to the reduced size of the LVCV's primary vortex. At the three other locations, the values are higher, which testify to increased losses leading to a reduced mass flow rate of the LVCV. Figure 15 brings out the values of Ψ for the LVCV at s = 50%. The higher value of Ψ for the CCV existing in the primary vortices compared to the LVCV is due to the influence of the vortex strength on the local pressure distribution there.

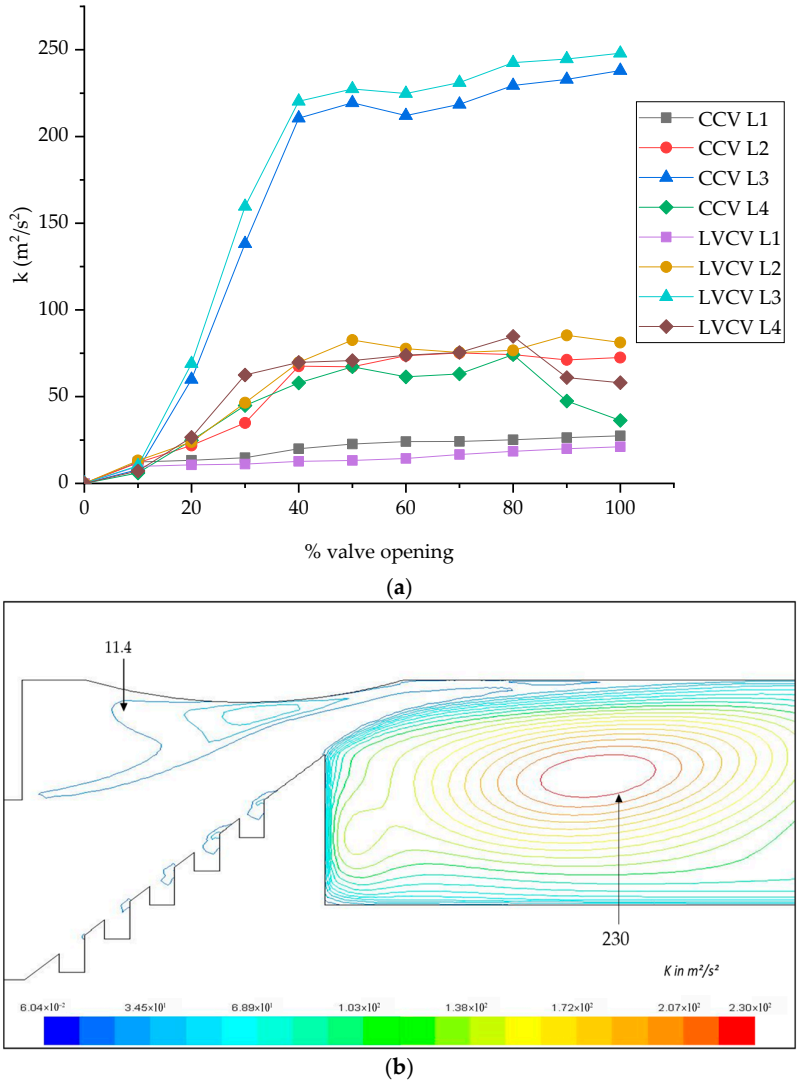

Figure 14. (**a**) Axisymmetric CFD analysis: (i) k values at the four locations shown in Figure 13a for the LVCV vs. % valve opening; (ii) k values at the four locations shown in Figure 5a for the CCV vs. % valve opening. (**b**) Axisymmetric CFD analysis: contours of k for the LVCV at 75% opening.

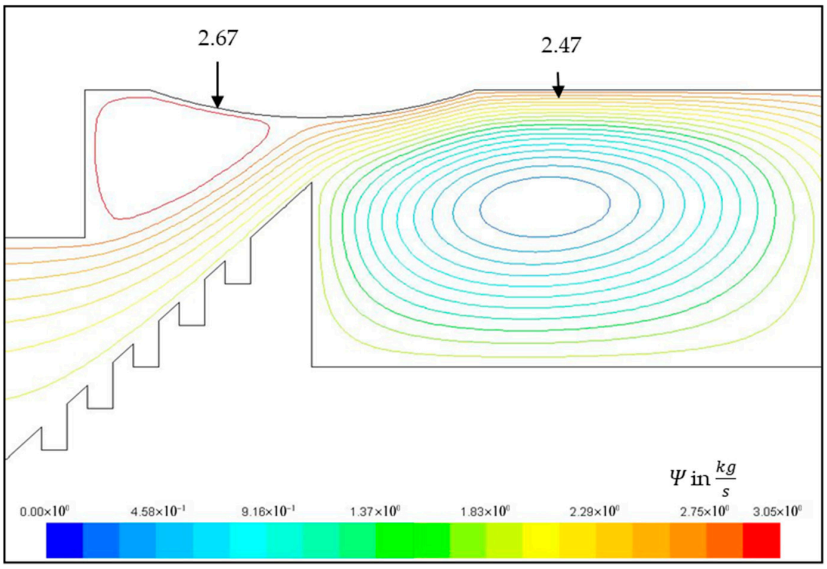

Figure 15. Axisymmetric CFD analysis: contours of stream function for LVCV at 50% opening.

Figure 16a represents the pressure contours for the LVCV at s = 25%, and Figure 16b displays the change in P_{vc} against different s values. It can be noticed that the pressure decreases continuously in the downstream direction for both valves. The static pressure values for the CCV are lower than those of their LVCV counterparts. At most of the locations up to the valve base, the pressure contours are normal to the local flow direction, implying that the pressure field is largely one dimensional. Yet, in the downstream domain following the valve base, the same view does not hold well. The above observations were noticed at all valve openings. The pressure drop occurring between the apex of the valve and the valve seat region for the LVCV is higher than that of the CCV due to the higher flow resistance offered by the labyrinth cavities. The same occurs between the valve seat region and the plane of the valve base, which is comparatively lower for the LVCV due to the combined effect of the labyrinths and venturi. Thus, it was observed that due to the application of the venturi and labyrinths, changes in vortex properties and velocity profiles occurred on either side of the valve seat plane. As far as the static pressure values at the vena contracta of the CCV and LVCV given in Figure 16b are concerned, those of the CCV are consistently lower, foretelling concurrent lower mass flow rates for the LVCV.

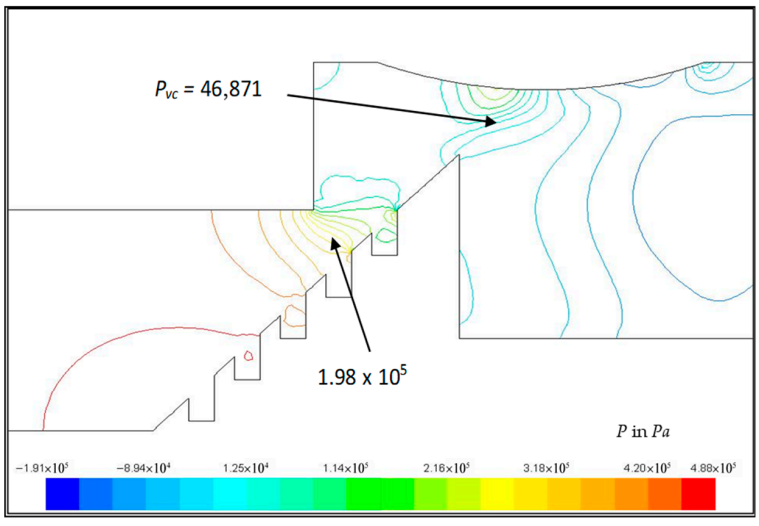

(**a**)

Figure 16. *Cont.*

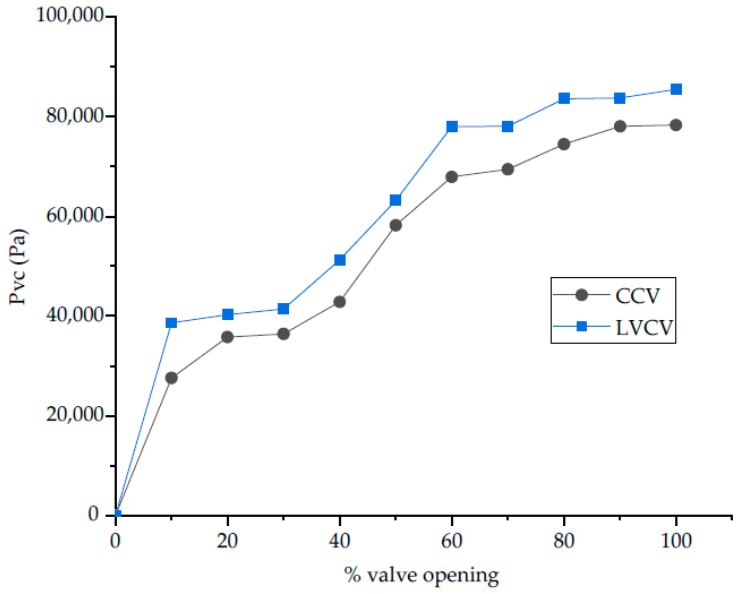

(**b**)

Figure 16. (**a**) Axisymmetric CFD analysis: contours of static pressure for LVCV at 25% opening. (**b**) Axisymmetric CFD analysis: vena contracta static pressures of CCV and LVCV vs. % valve opening.

Figure 17, showing the mass flow of the LVCV at all valve openings obtained from CFD, depicts that the LVCV has close linear flow characteristics. It was intended to validate the mass flow predicted by CFD against experimental data so as to apply the numerical analysis as a tool for valve design optimization.

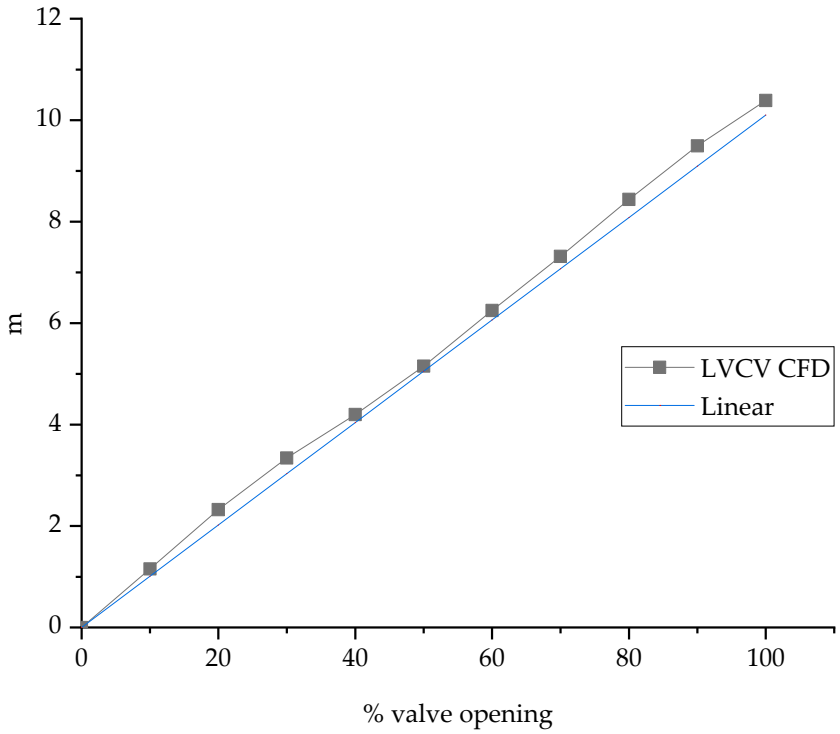

Figure 17. Mass flow ratio vs. % valve opening for LVCV.

3. Validation of CFD Results by Experiment

3.1. Experimental Setup

The experimental setup fabricated for flow testing through the conical valves is shown in Figure 18. It consists of a closed-loop water circuit, which includes a water tank with a strainer and a centrifugal pump capable of developing a total gauge pressure of over 6 bar. The pump discharges to a vertical pipe from which a bypass line branches off. The tank maintains the water temperature at the predominantly existing daytime ambient value of 35 °C. A pressure sensor, Pi, already calibrated against dead weights, measured the inlet static pressure. The exit pressure P_e at the short exit pipe was invariably atmospheric. The pressure sensor used is of analog type and is made of stainless steel. The sensor provides a digital output in the range of 0.5 V to 4.5 V, which is used to measure the pressure of the water entering the test setup. The pressure values were often verified by manometers to reduce the margin of uncertainty, and the ambiguity of the pressure gauge was observed to be ±2500 Pa. The bypass valve can be adjusted to maintain the inlet pressure at a constant value. The stem of the valve throttling the flow was extended and passed coaxially through a hard and thick acrylic glass tube, which enabled visualization of the flow. The stem was connected to a graduated wheel, which could be rotated to move the valve. The valve stroke measured from the graduations on the wheel were cross-verified against a dial indicator, making the uncertainty associated with valve opening negligible. The errors related to concentricity of the valve with respect to the centerline were estimated to be in the order of 3%.

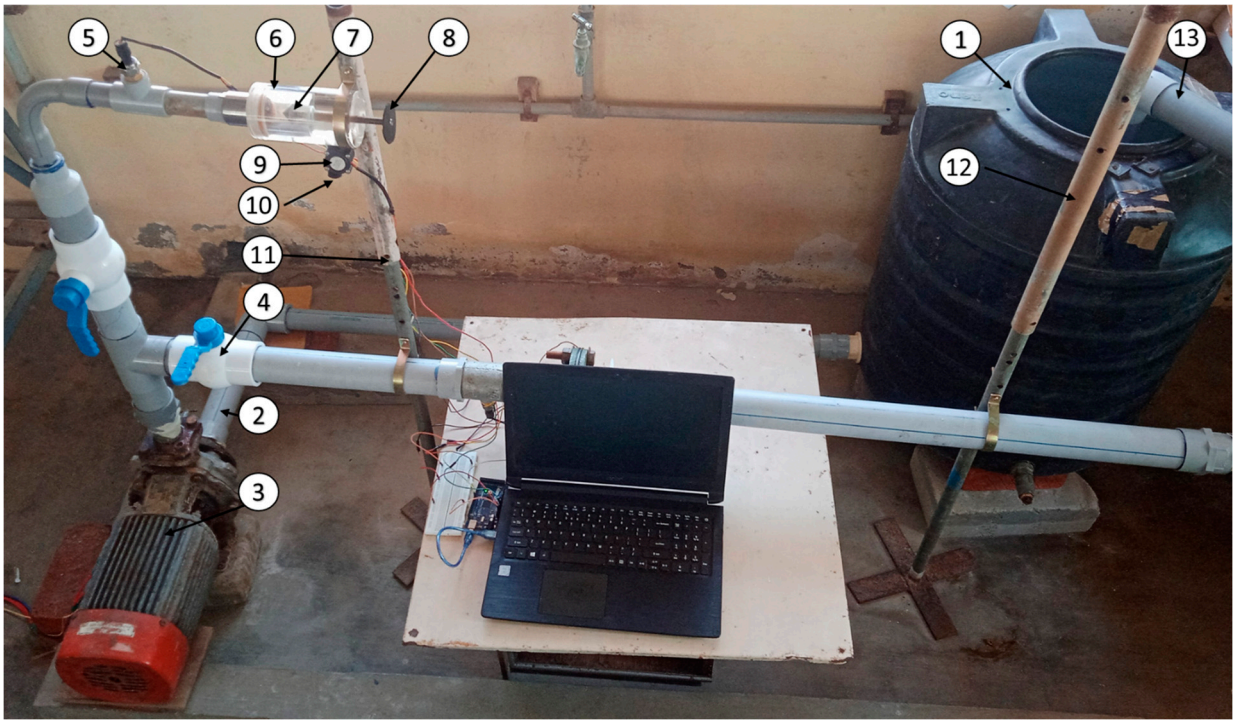

1. Water tank
2. Inlet pipe
3. Pump
4. Bypass valve
5. Pressure sensor Pi
6. Glass tube
7. Conical valve
8. Valve gap adjusting wheel
9. Digital flow sensor
10. Exit to atmosphere
11. Valve stand
12. Bypass stand
13. Bypass water pipe

Figure 18. Photographic view of experimental setup.

3.2. Experimental Results for CCV and LVCV

The experimental mass flow rates reported in the paper are obtained from the output of a digital water flow sensor setup. The flow sensor used is of the Hall effect type, which provides a digital output in the range of 1.65 to 5.5 V. The output signal from the sensor is sent to the Arduino, where the voltage value is decoded into the flow rate according to the pre-loaded program. The values were validated by collecting the discharge in a large calibrated collecting tank. Repeated measurements and statistical investigations revealed a maximum variation of ±1% between the mass flow data collected by both methods. The combined effect of the above-mentioned deviations was revealed during repeatability tests on mass flow measurement and found to be around ±4%. Figure 19 provides the mass flow ratios obtained from experimental testing at various valve openings of the CCV and LVCV, along with the corresponding CFD values. The mass flow obtained by CFD consistently exceeded the experimental values [21] at all the openings. The axisymmetric CFD and experimental results closely matched up to about 30% valve opening, but deviations kept creeping thereafter, with the maximum error of 24% occurring at 100% valve opening, looking a shade higher. Recollecting that the direction of actual flow discharge was not axial, the flow losses had disbursed well beyond the zone of the valve seat. It is possible that the high magnitude of the maximum error could be due to the flow field transitioning more into a three-dimensional pattern, particularly at larger valve openings. Axisymmetric analysis was carried out assuming the flow exits in the axial direction. As seen in the experimental setup in Figure 18, the flow enters the valve axially and turns down perpendicularly at the discharge side. Three-dimensional CFD analysis brings the simulation results in good agreement with the experimental data [22,23]. To make simulations more realistic, 3-D CFD modeling of the flow passage at 100% valve opening alone was also carried out.

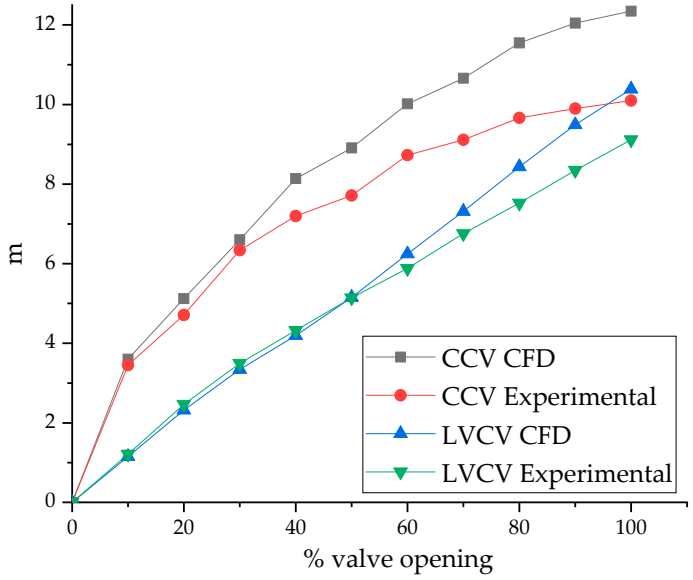

Figure 19. Experimental and CFD mass flow ratio vs. % valve opening for CCV and LVCV.

3.3. Improved Numerical Prediction by 3-D Analysis

The three-dimensional model of the valve is generated with conditions of axial inlet and exit with a right-angle bend. Figure 20 shows the mesh obtained from the ANSYS software for the CCV at the 100% opening condition. At the grid independent condition, the 3-D mesh obtained with the inflation option had 290,548 tetrahedral elements of size 2 mm. Figure 21a shows velocity vectors, velocity at L2, and vena contracta for the CCV at the 100% valve opening predicted by 3-D analysis. Values of velocities at homologous locations provided by axisymmetric and 3-D CFD analyses are given in Table 5. Though the

difference in values is slender, looking at Figures 5a and 21a, it can be noticed that while the primary vortices in both of them are nearly unchanged, the secondary vortex in Figure 21a is flatter, bigger, and stronger than its counterpart in Figure 5a. The altered flow pattern can lead to increased losses/flow resistance, resulting in a decrease in the predicted mass flow rate, which primarily explains the higher-valued flow prediction of the axisymmetric CFD model at the upper percentages of valve openings. Though the 3-D simulation still over-predicted mass flow, the maximum error at the 100% valve opening came down to 13.8% compared to the 24% deviation for the axisymmetric analysis of the CCV.

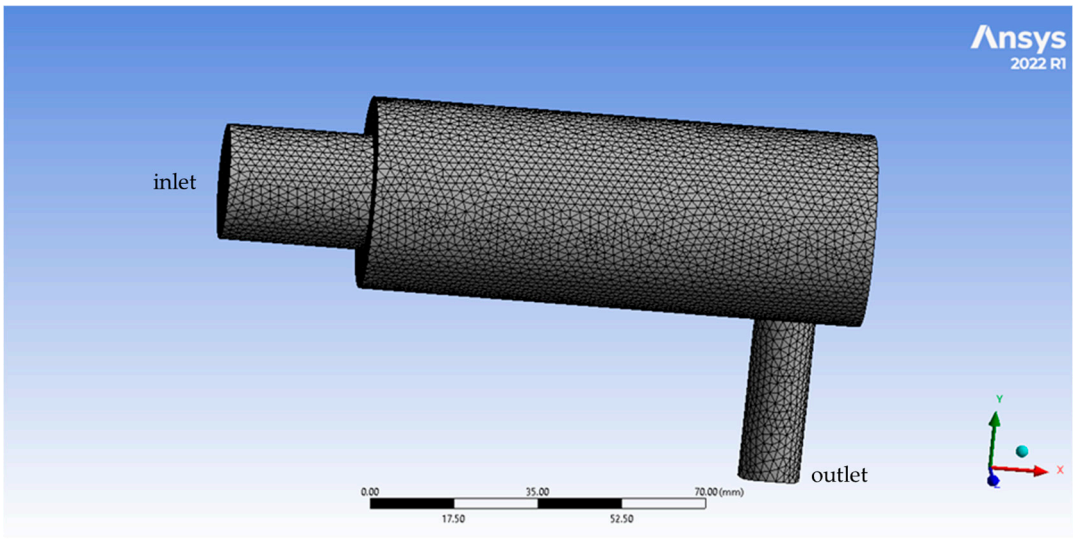

Figure 20. Three-dimensional computational mesh for 100% valve opening of CCV.

Table 5. CFD-predicted velocity values at four locations of CCV at 100% valve opening obtained by axisymmetric and 3-D analysis.

Sl. No.	Location	Velocity Values (m/s)	
		Axisymmetric	3-D
1	L1	2.46	0.81
2	L2	32.30	30.90
3	L3	3.82	2.50
4	L4	12.92	12.30
5	Vena Contracta	36.20	35.70

Figure 21b shows the velocity vectors, velocity at L2, and vena contracta obtained from the 3-D CFD analysis carried out at the 100% valve opening position for the LVCV. Values of velocities at homologous locations predicted by axisymmetric and 3-D CFD analyses are given in Table 6. Here again, although the difference in values is slight, by observing Figures 13a and 21b, it can be noted that noticeable changes pertain to the pattern of the secondary vortex only. Unlike a single large secondary vortex predicted by axisymmetric CFD analysis of the LVCV as seen in Figure 13a, the 3-D CFD analysis of the LVCV brings out a somewhat smaller secondary vortex, as noted in Figure 21b, but with additional dispersals. This is mainly attributed to the change of direction of water exit, assumed to be axial for axisymmetric analysis, into radially downwards in the 3-D analysis, which is much closer to the actual experimental situation.

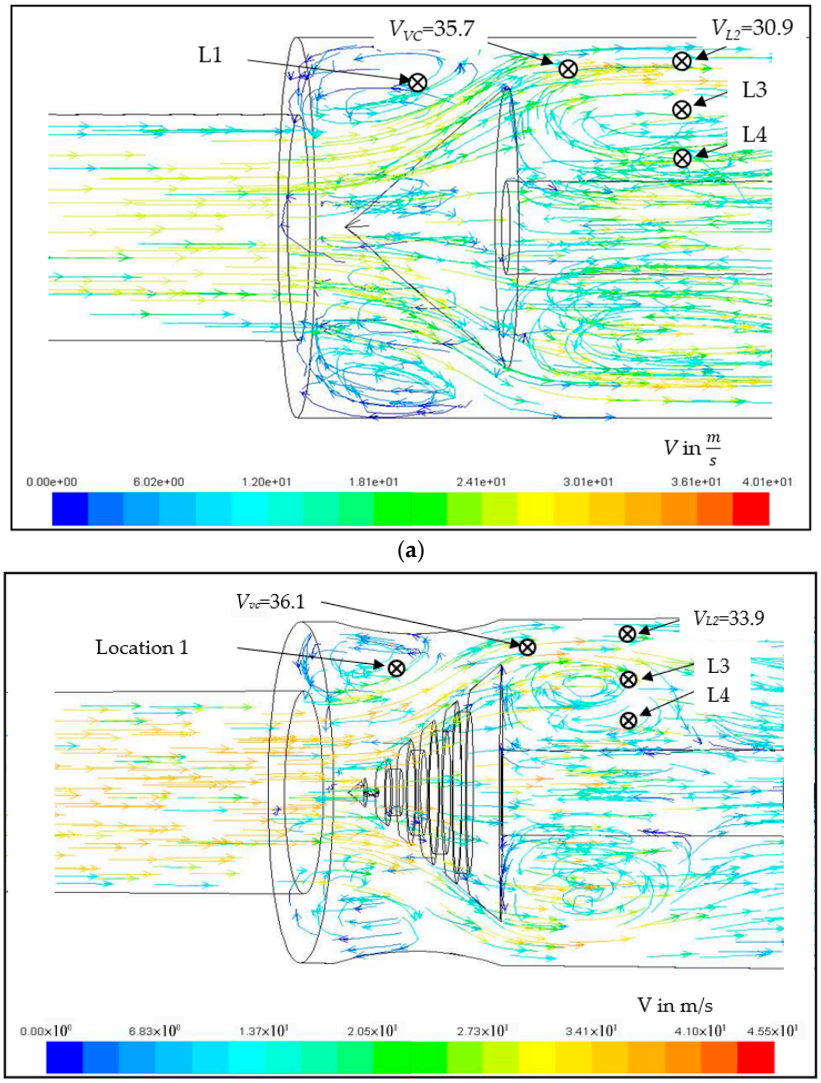

Figure 21. (**a**) The 3-D CFD analysis: velocity vectors, V_{vc} and V_{L2} for the CCV at the 100% opening. (**b**) The 3-D CFD analysis: velocity vectors, V_{vc} and V_{L2} for the LVCV at the 100% opening.

Table 6. CFD-predicted velocity values at four locations of LVCV at 100% valve opening obtained by axisymmetric and 3-D analysis.

Sl. No.	Location	Velocity Values (m/s)	
		Axisymmetric	3-D
1	L1	2.15	1.30
2	L2	34.11	33.90
3	L3	4.44	4.10
4	L4	19.33	18.95
5	Vena Contracta	36.90	36.10

In reality, the 90° change in flow direction in the flow exit can be speculated to have made the free shear layers shed from the secondary vortex and form an elongated downstream wake zone, as found in Figure 21b. The associated combined losses might have been more than that for the secondary vortex predicted by axisymmetric CFD analysis, seen in Figure 13a. This explains the reduction in error in the 3-D CFD-predicted mass flow

at the 100% valve opening of the LVCV to 7.47% compared to 14.3% encountered with the axisymmetric prediction.

4. Conclusions

Control valves with linear flow characteristics are of utmost importance in various industrial applications with flow control requirements. Conventional Conical Valves (CCVs) have quick opening characteristics with little effect on the flow rate through them. Flow control in the CCV was enhanced by introducing a venturi in the valve assembly and incorporating labyrinth grooves into the body of the conical valve. These novel design modifications led to the development of the Labyrinth Venturi Conical Valve (LVCV). Discharge characteristics of these conical valves operating at a 5 bar (gauge) inlet static pressure, axial inlet, and radial outlet were determined using axisymmetric and three-dimensional CFD simulations. Four distinct location points along with primary and secondary vortices were identified in the flow region of both the CCV and LVCV models. The profiles of velocity, turbulent kinetic energy, stream function, and pressure at the four location points were plotted against percentage valve openings, and the flow physics behind the improved flow linearity of the LVCV was discussed. The numerical predictions were in close agreement with the experimental results at lower percentage valve openings. Mass flow predictions from the 3-D CFD analysis were closer to the corresponding axisymmetric analysis results, as the former was closer to experimental conditions. It was illustrated that the implementation of venturi geometry on the valve casing and labyrinth grooves on the tapering plug of the conical valve jointly contributed to linearizing the flow. Under the investigated operating conditions, the LVCV's discharge was close to linear until around 80% opening of the valve.

Author Contributions: S.P.A. formulated the concept, outlined the CFD/experimental schemes, and prepared the manuscript. B.V. carried out the CFD and experimental investigations. T.S. validated the CFD and experimental results and intellectually revised the manuscript. G.R.M. carried out the correlation of the results. All authors have read and agreed to the published version of the manuscript.

Funding: This research received no external funding.

Data Availability Statement: The original contributions presented in this study are included in the article. Further inquiries can be directed to the corresponding author.

Acknowledgments: The inspiration for this study was derived from a completed sponsored research project from the Indira Gandhi Centre for Atomic Research, Kalpakkam, Govt. of India, and the assistance of R.J. Sathesh and K. Arunkumar and support extended by MSEC are thankfully remembered.

Conflicts of Interest: Author Gurunathan Rajaguru Manikandan was employed by the company Tata Consultancy Services. The remaining authors declare that the research was conducted in the absence of any commercial or financial relationships that could be construed as a potential conflict of interest.

Nomenclature

The following nomenclatures are used in this manuscript.

g	Acceleration due to gravity, (m/s^2)
k	Turbulent kinetic energy, (m^2/s^2)
L_1	Location 1
m	Mass flow ratio of water passing through the valve
P_i	Valve inlet pressure, (Pa)
P_e	Fully recovered valve exit pressure, (Pa)
P_{vc}	Static pressure at vena contracta, (Pa)
s	Stroke length (mm) or % opening of the valve
V	Velocity, (m/s)

V_{vc}	Velocity of water at the vena contracta, (m/s)
ρ	Mass density, (kg/m^3)
Ψ	Stream function, (kg/s)
ϕ	Diameter

Abbreviations

The following abbreviations are used in this manuscript.

CPU	Central Processing Unit
SIMPLEC	Semi-Implicit Method for Pressure Linked Equations-Consistent
RAM	Random Access Memory
CCV	Conventional Conical Valve
VCV	Venturi Conical Valve
LVCV	Labyrinth Venturi Conical Valve

References

1. Leephakpreeda, T. Design factors for "linear" ball valve: Theoretical and experimental studies. *Songklanakarin J. Sci. Technol. (SJST)* **2005**, *27*, 353–361.
2. Davis, J.A.; Stewart, M. Predicting Globe Control Valve Performance—Part I: CFD Modeling. *J. Fluids Eng.* **2002**, *124*, 772–777. [CrossRef]
3. Daines, R.; Ahuja, V.; Hosangadi, A.; Shipman, J.; Moore, A.; Sulyma, P. Computational Modeling of Liquid and Gaseous Control Valves. In Proceedings of the 41st AIAA/ASME/SAE/ASEE Joint Propulsion Conference & Exhibit, Tucson, AZ, USA, 10–13 July 2005.
4. Chern, M.J.; Wang, C.C. Control of volumetric flow rate of ball valve using V-port. *J. Fluids Eng.* **2004**, *126*, 471–481. [CrossRef]
5. Victor Perr, J. Conical Air Flow Valve Having Improved Flow Capacity and Control. CN102906656A, 26 March 2011.
6. Jalil, J.M.; Ahmed, S.T.; Xue, Y.; Ghadhban, S.A. Experimental and numerical investigation of fluid flow of truncated conical poppet valve. *Int. J. Fluid Power* **2015**, *16*, 25–34. [CrossRef]
7. Jin, Z.J.; Gao, Z.X.; Zhang, M.; Liu, B.Z.; Qian, J.Y. Computational fluid dynamics analysis on orifice structure inside valve core of pilot-control angle globe valve. *Proc. Inst. Mech. Eng. C J. Mech. Eng. Sci.* **2017**, *232*, 2419–2429. [CrossRef]
8. Vaughan, N.D.; Johnston, D.N.; Edge, K.A. Numerical Simulation of Fluid Flow in Poppet Valves. *Proc. Inst. Mech. Eng. C J. Mech. Eng. Sci.* **1992**, *206*, 119–127. [CrossRef]
9. Tan, L.; Xie, H.; Chen, H.; Yang, H. Structure optimization of conical spool and flow force compensation in a diverged flow cartridge proportional valve. *Flow Meas. Instrum.* **2019**, *66*, 170–181. [CrossRef]
10. Hong, G.; Xin, F.; Hua-Yong, Y.; Tetsuhiro, T. Numerical investigation of cavitating flow behind the cone of a poppet valve in water hydraulic system. *J. Zhejiang Univ.-Sci. A* **2002**, *3*, 395–400. [CrossRef]
11. Li, J.; Fu, X.; Yan, S. Simulation and Experimental Investigation of a New Type of Combined Seal Structure. *J. Fluids Eng.* **2021**, *143*, 051503. [CrossRef]
12. Roy, V.; Guibault, F.; Vu, T. Validation of a CFD model for hydraulic seals. *Int. J. Fluid Mach. Syst.* **2009**, *2*, 400–408. [CrossRef]
13. Qin, H.; Lu, D.; Zhong, D.; Wang, Y.; Song, Y. Experimental and numerical investigation for the geometrical parameters effect on the labyrinth-seal flow characteristics of fast reactor fuel assembly. *Ann. Nucl. Energy* **2020**, *135*, 106964. [CrossRef]
14. Morgan, N.R.; Wood, H.G.; Untaroiu, A. Design of Experiments to Investigate Geometric Effects on Fluid Leakage Rate in a Balance Drum Seal. *J. Eng. Gas Turbine Power* **2016**, *138*, 072506. [CrossRef]
15. Mamatov, S.; Shin, D.; Park, S.S. Investigation on Leakage Characteristics of Two Kinds of Injection-type Shaft Seals Using CFD. *Int. J. Fluid Mach. Syst.* **2020**, *13*, 635–645. [CrossRef]
16. Duan, A.; Wang, C.; Xu, J.; Gao, S.; Liu, X.; Jin, H. Experiment and numerical simulation investigation on cavitation evolution and damage in the throttling section of pressure reducing valve. *Energy Sci. Eng.* **2022**, *10*, 2348–2366. [CrossRef]
17. Lin, Z.; Wang, H.; Shang, Z.; Cui, B.; Zhu, C.; Zhu, Z. Effect of cone angle on the hydraulic characteristics of globe control valve. *Chin. J. Mech. Eng.* **2015**, *28*, 641–648. [CrossRef]
18. Asok, S.P.; Sankaranarayanasamy, K.; Sundararajan, T.; Vaidyanathan, G.; Udhaya Kumar, K. Pressure drop and cavitation investigations on static helical-grooved square, triangular and curved cavity liquid labyrinth seals. *Nucl. Eng. Des.* **2011**, *241*, 843–853. [CrossRef]
19. Wang, H.; Zhao, Y.; Wang, J.; Kong, X.; Liu, H.; Li, K. Numerical simulation of flow characteristics for a labyrinth passage in a pressure valve. *J. Hydrodyn. B* **2016**, *28*, 629–636. [CrossRef]
20. Joachimmiak, D.; Krzyslak, P. Analysis of the Gas Flow in a Labyrinth Seal of Variable Pitch. *J. Appl. Fluid Mech.* **2019**, *12*, 921–930. [CrossRef]

21. Strmčnik, E.; Majdič, F. Comparison of leakage level in water and oil hydraulics. *Adv. Mech. Eng.* **2017**, *9*, 1687814017737723. [CrossRef]
22. Upendra, R.; Manoj, P.; Viswanath, A.K.; Prerana, N.; Tikendra, N.V.; Arivalagan, P. A numerical investigation on a diesel engine characteristic fuelled using 3D CFD approach. *Fuel* **2024**, *368*, 131488. [CrossRef]
23. Cană, P.; Ripeanu, R.G.; Pătîrnac, I.; Diniță, A.; Tănase, M. Investigating the Impact of Operating Conditions on Relief Pressure Valve Flow through CFD and Statistical Analysis. *Processes* **2023**, *11*, 3396. [CrossRef]

Disclaimer/Publisher's Note: The statements, opinions and data contained in all publications are solely those of the individual author(s) and contributor(s) and not of MDPI and/or the editor(s). MDPI and/or the editor(s) disclaim responsibility for any injury to people or property resulting from any ideas, methods, instructions or products referred to in the content.